Supplement for

"Field Observations Reveal Substantially Higher Scattering Refractive Index in Secondary Versus Primary Organic Aerosols"

Junlin Shen[1], Li Liu[2], Fengling Yuan[1], Biao Luo[1], Hongqing Qiao[1], Miaomiao Zhai[1], Gang Zhao[3], Hanbing Xu[4], Fei Li[5], Yu Zou[2], Tao Deng[2], Xuejiao Deng[2], Ye Kuang[1]

[1] Institute for Environmental and Climate Research, College of Environment and Climate, Jinan University, Guangzhou, 511443, Guangdong, China

[2] Guangzhou Institute of Tropical and Marine Meteorology of China Meteorological Administration, GBA Academy of Meteorological Research, Guangzhou, 510640, China.

[3] Key Laboratory of Ecology and Environment in Minority Areas, Minzu University of China, National Ethnic Affairs Commission, Beijing,100081, China

[4] School of Computer Science and Engineering, Sun Yat-Sen University, Guangzhou, 510275, Guangdong, China

[5] Xiamen Key Laboratory of Straits Meteorology, Xiamen Meteorological Bureau, Xiamen, 361012, Fujian, China

Correspondence: Ye Kuang (kuangye@jnu.edu.cn) and Li Liu (liul@gd121.cn)

Summary: 16 pages, 6 method sections, 11 figures

Contents of this file

1. Calibration for SP2

Calibration work was conducted to study the positive monotonic relationship between aerosol scattering coefficient and scattering peak signal measured by SP2. The relationship is described by the following:

$$C_{sca} = K1_{sca} \times P_{sca} + K2_{sca} \quad (1)$$

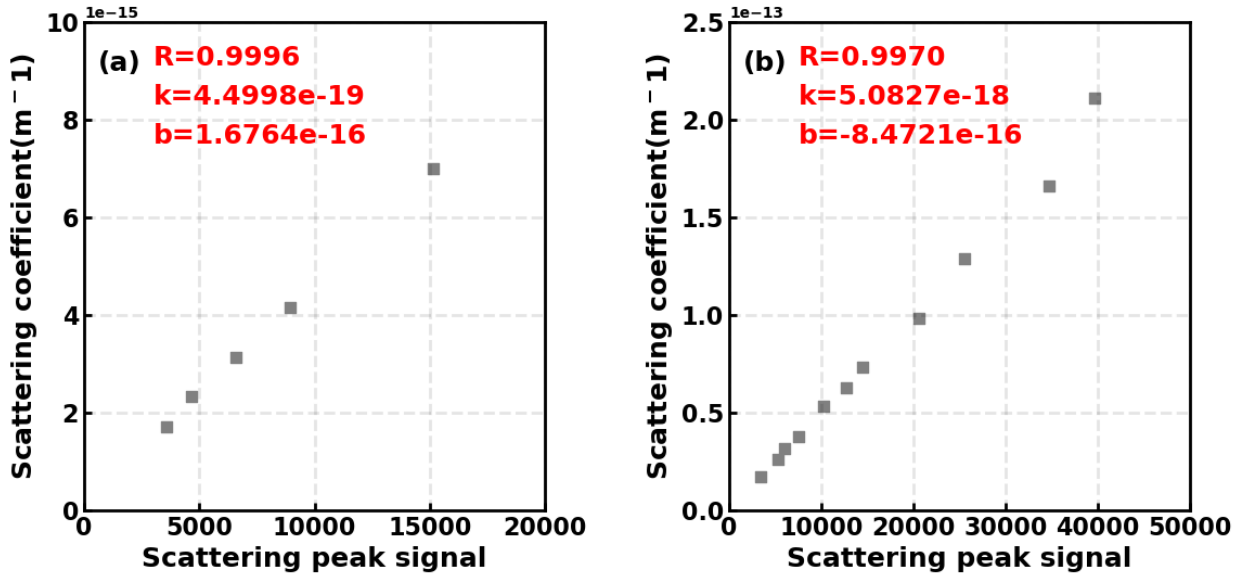

Figure S1. Comparison between measured scattering coefficient and scattering peak signal from **(a)** high gain channel and **(b)** low gain channel of SP2.

where C_{sca} is the particle scattering coefficient and P_{sca} is peak of scattering signal. For SP2, the method for observing scattering signal is recording time series of scattering signal through both high gain and low gain channel. Ammonium sulphate, with a refractive index of $1.53 + 10^{-7}$i was used for calibration. The DMA was set to scan aerosol diameters ranging from 80nm to 500nm. For each selected diameters, corresponding particle scattering coefficient was calculated by Mie theory. The results from both high gain and low gain channels are displayed in FigureS1 (a) and (b), with correlation coefficient reaching more than 0.99. The relationship between aerosols scattering coefficient and scattering peak signal can be described as:

$$C_{sca} = 4.499^{-15} \times P_{sca} - 1.676^{-12} \quad (1)$$

$$C_{sca} = 5.083^{-14} \times P_{sca} - 8.472^{-12} \quad (2)$$

On the basis of observed scattering of particles, and aerosol diameters determined by the DMA, real part of aerosol refractive index of BC-free aerosols at 1064 nm can be retrieved using the method proposed by Zhao et al. (2019b).

2. The source apportionment of volume size distribution

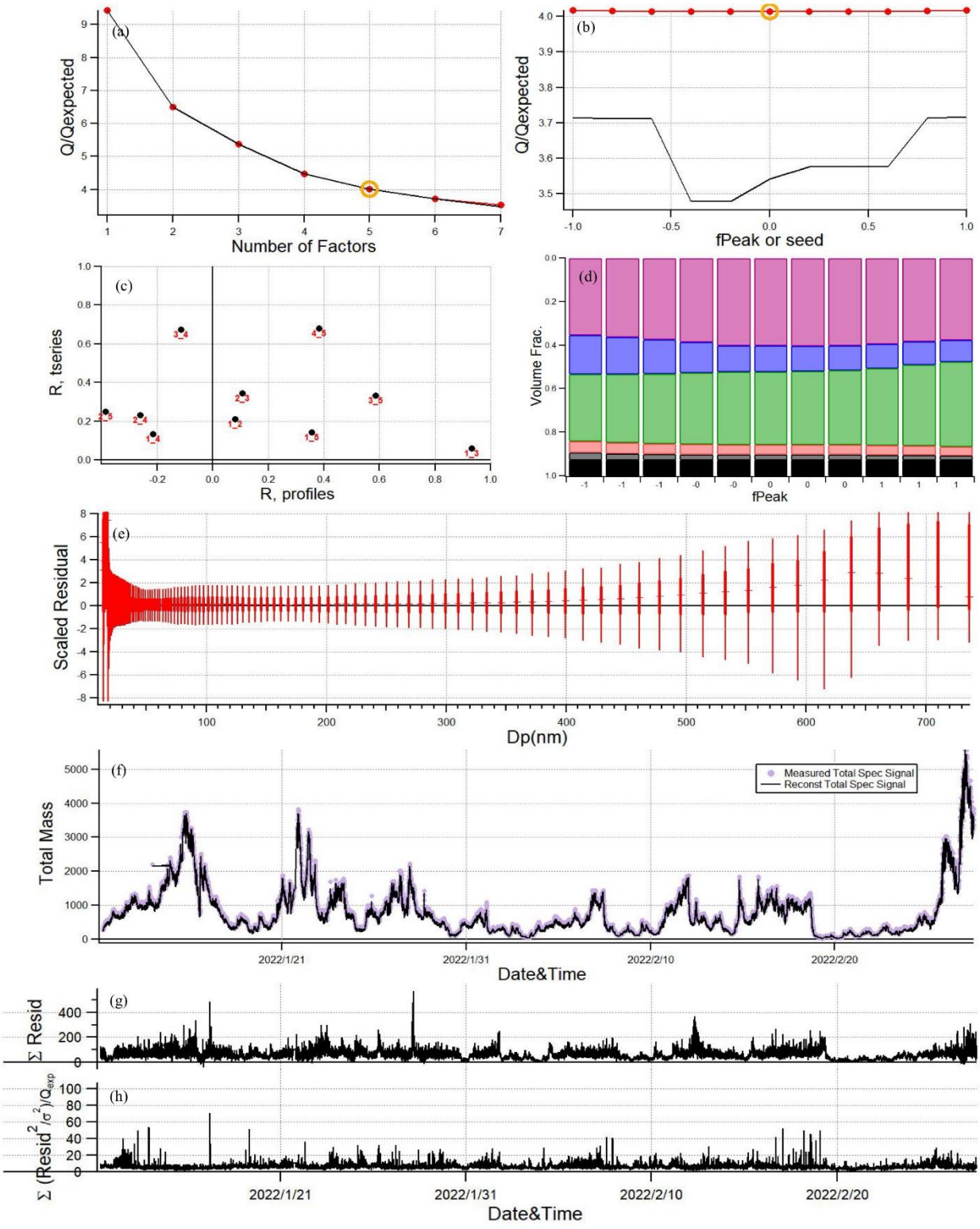

Figure S2. Diagnostic plots of the 5-factor solution in the unconstrained PMF.

The PMF technique was applied to resolve the particle number size distribution measured by the SMPS into different source factors. The diagnostics analysis, as presented in Figure S2,

performed that number of 3-6 could be possible solution. It was determined that five factors solution was the best solution. The four factors solution failed to split two mutual independent factors. For example, the factor 2 of 5 factor solutions are not resolved. This factor at relatively larger diameter ranges is usually associated with aqueous secondary aerosol formations (Kuang et al., 2020) While six factors solution over split factors, with factor 6 contributing negligibly to aerosol volume. The volume size distribution, diurnal variation and correlation coefficients with chemical components for four, five and six factors solutions are displayed in figure S3. Four factors solution was unable to split the factor that prominently profiles the volume size distribution in the 300nm to 700nm range. In contrast, in five factors solution, factor 2 exhibited a distinct correlation coefficient with chemical components compared to the other factors, particularly with SOA (LOOA and MOOA,$R = 0.87$). However, when an additional sixth factor was included, corresponding characteristics show less pronounced. Therefore, we suggest that five factors can explain dataset well.

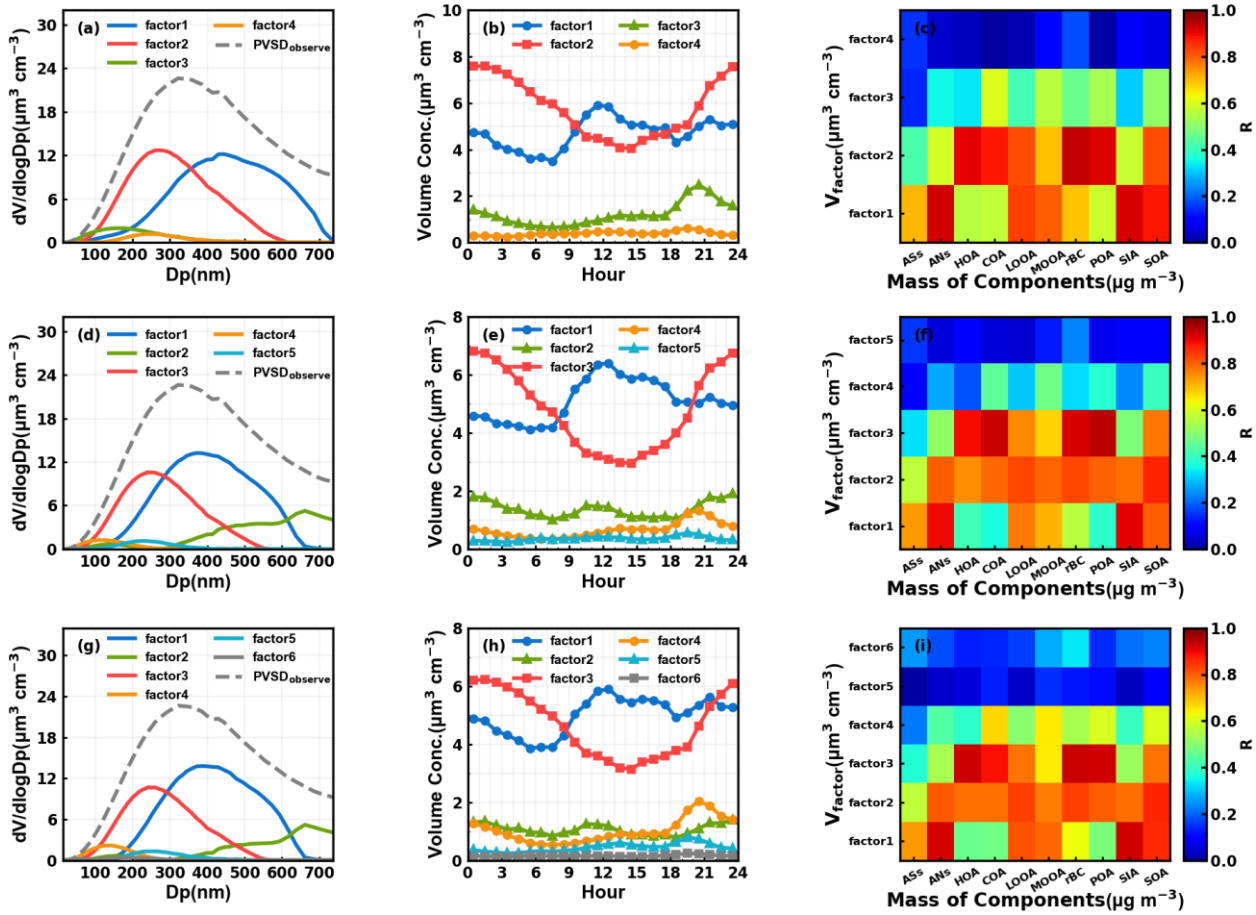

Figure S3. The volume size distribution, diurnal volume variation and correlation coefficient with chemical components of 3-5 factors solution.

3. The relationships between dry state aerosol scattering of PM_1 and TSP

Kuang et al. (2024) developed an advanced aerosol-cloud sampling system designed to measure fog and cloud activation processes with this system include inlets of PM_1, $PM_{2.5}$ and TSP and the sampling flow switch automatically between these three inlets. Under subsaturated conditions (not in cloud and fog cases), this system could be used to measure scattering coefficients of PM_1, $PM_{2.5}$ and TSP aerosols if a nephelometer is placed downstream of this sampling system. This system coupled with two nephelometers (one without drying, and another one with sampling RH dried to below 15%) and other instruments was placed in Panyu station (Tan et al., 2013) of Institute of Tropical and Marine Meteorology, Guangzhou, China, since 24th May. Time duration for each inlet is 10 minutes and switch in the order if PM_1, TSP and $PM_{2.5}$. Linear interpolation was applied to all aerosol scattering measurements of PM_1 to match the time of TSP measurements. Results of Xu et al. (2024) demonstrated that the dry-state PM_1 measurements would be affected by

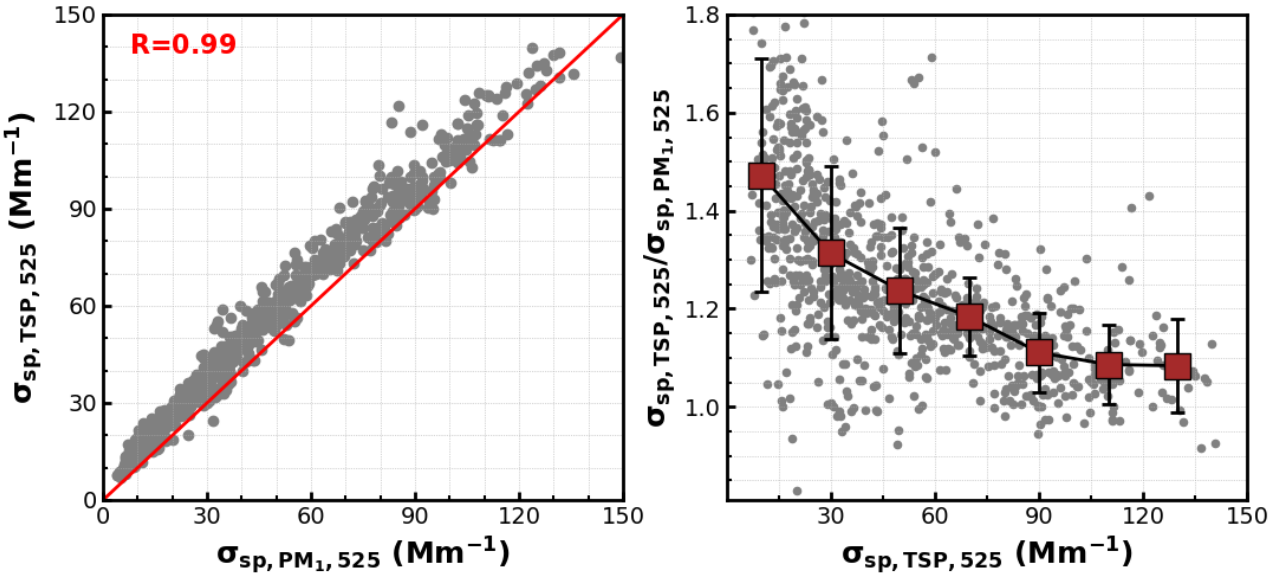

Figure S4. **(a)** Comparison dry-state aerosol scattering coefficients at 525 nm between inlets of PM_1 ($\sigma_{sp,PM_1,525}$) and TSP ($\sigma_{sp,TSP,525}$); **(b)** The ratio $\sigma_{sp,TSP,525}/\sigma_{sp,PM_1,525}$ under different $\sigma_{sp,TSP,525}$ levels.

aerosol hygroscopic growth when RH is higher than 60%. Therefore, data points with RH smaller than 60% (from 24th May to 19th August) was used to retrieve relationships between aerosol scattering of dry-state PM_1 and TSP ($\sigma_{sp,PM_1,525}$ vs $\sigma_{sp,TSP,525}$) as shown in Fig.S4. Fig.S4a shows that aerosol scattering of dry-state PM_1 and TSP correlate highly with the correlation coefficients reaches 0.99, however their ratio varies depending on aerosol scattering levels as shown in Fig.S4b. The ratio $\sigma_{sp,TSP,525}/\sigma_{sp,PM_1,525}$ could reaches as high as 1.5 when $\sigma_{sp,TSP,525}$ is smaller than 15 Mm^{-1} with the standard deviations could be higher than 0.2, however, the $\sigma_{sp,TSP,525}/\sigma_{sp,PM_1,525}$ reduces as nearly a constant of 1.08 for $\sigma_{sp,TSP,525}$ higher than 90 Mm^{-1} with standard deviation of about 0.05. This relationship allows us to establish an average correction curve as a function of $\sigma_{sp,TSP,525}$, and 1.08 is used for $\sigma_{sp,TSP,525}$ higher than 130 Mm^{-1}.

4.The calculating procedures of aerosol scattering coefficient simulations

As discussions presented in Sect 2.3, aerosol particle number size distribution (PNSD), BC mass size distribution and mixing state, as well as refractive index of BC and non-BC (treated as almost pure scattering at 525 nm where light absorption of brown carbon is small) is needed for the aerosol scattering simulations. Rext (mass fractions of externally mixed BC in total BC mass) of 0.56 and Rcsm (number fractions of coreshell mixed particles in total non-external BC particles, including BC containing coreshell mixed BC and pure scattering) of 0.13 are used to represent BC mixing state. The BC mass concentrations measured (M_{BC}) by AE_{33} is distributed to different diameters using the lognormal distribution with the D_g of 258 and σ_g of 1.69:

$$\frac{dM_{BC}(Dp)}{dlogDp} = \frac{M_{BC}}{\sqrt{2\pi}\log(\sigma_g)} \cdot \exp\left(-\frac{[\log(D_p)-\log(D_g)]^2}{2\log(\sigma_g)^2}\right) \quad (1)$$

Three types of aerosols were included in this simulation: (1) BCe, externally mixed BC particles, (2) BCc, BC-containing coreshell particles; (3) PS, BC-free pure scattering particles. For each type of particles, the aerosol scattering can be represented as:

$$\sigma_{sp,type}(\lambda) = \int Q_{sp,type,nep}(Dp, \widetilde{m}, \lambda) * \left(\frac{\pi Dp^2}{4}\right) * N(logDp, type) * dlogDp \quad (2)$$

where scattering efficiency ($Q_{sca,type,neph}$) that considered the truncation error of nephelometer and non-ideality of light source is a function of particle diameter (Dp), refractive index $\widetilde{m}$ and wavelength (λ) based on the basis of Mie theory, N(logDp, type) is the particle number size distribution (PNSD) of corresponding aerosol type. The refractive index of BC is 1.96 – 0.66i which is consistent with Ma et al. (2011), and refractive index of non-BC components is m_r – 10^{-7}i, and 10^{-7} for the imaginary part is recommended by (Wex et al., 2002) , m_r is the parameter that needs to be retrieved in the closure.

The $Q_{sca,type,neph}$ was calculated by integrating the scattering intensity function $|S(\theta, x, \widetilde{m})|$ from 0° to 180°:

$$Q_{sca,type,neph} = \frac{1}{x^2}\int_0^{180} |S(\theta, x, \widetilde{m})|^2 \sin\theta \times Z_{ts}(\theta)\, d\theta \quad (3)$$

Where $x = \pi D_p/\lambda$, $Z_{ts}(\theta)$ is scattering sensitivity functions that counts for angel truncation errors and light source non-ideality of the Aurora 3000 nephelometer which was reported by Müller et al. (2011) through calibration experiment. Note that, for the BCc type particles, the $|S(\theta, x, \widetilde{m})|$ can be calculated using the BHCOAT code (Cheng et al., 2008).

For the BCe type particles, $\mathrm{N(logDp)_{BCe}}$ can be derived as:

$$\mathrm{N(logDp)_{BCe}} = \frac{dM_{BC}(Dp)\times \mathrm{Rext}}{dlogDp\times\rho_{BC}\times\frac{\pi}{6}\times {D_p}^3} \quad (4)$$

Where ρ_{BC} is density of BC and set as 1 g/cm^3 for BC on the basis of results of Zhou et al. (2022)

Then $\mathrm{N(logDp)_{BCc}}$ and $\mathrm{N(logDp)_{PS}}$ can be derived as:

$$\mathrm{N(logDp)_{BCc}} = (N(logDp) - \mathrm{N(logDp)_{BCe}}) \times Rcsm \quad (5)$$

$$\mathrm{N(logDp)_{PS}} = (N(logDp) - \mathrm{N(logDp)_{BCe}}) \times (1 - Rcsm)$$

The core diameter of BCc particle can be calculated as:

$$D_c = (\frac{6*M_{BC}(Dp)*(1-Rext)}{\rho_{BC}*\pi*\mathrm{N(logDp)_{BCc}}})^{\frac{1}{3}}$$

On the basis of above formulas, aerosol scattering coefficient at 525 nm for each type of aerosols that have corrected to the nephelometer case can be simulated, and thus the total aerosol scattering coefficient at 525 nm of the nephelometer case ($\sigma_{sp,neph,525}$) can be calculated as:

$$\sigma_{sp,neph}(525) = \sigma_{sp,neph,BCe}(525) + \sigma_{sp,neph,BCc}(525) + \sigma_{sp,neph,PS}(525) \quad (6)$$

5. Sensitivity test associated with aerosol scattering coefficients and m_{rc525} retrieval with different input parameters

As introduced in Sect.S4, aerosol scattering is influenced by many factors such as refractive index, mixing state, BC mass size distributions and BC mass concentration. A sensitivity analysis on the basis of measured average PNSD, BC mass size distributions and mixing sates during the first campaign is conducted to explore impacts of these parameters on aerosol scattering coefficient at 525 nm ($\sigma_{sp,sim}$) through perturbating these input parameters. These parameters include the density of BC, BC refractive index, BC mass concentration, real part of the refractive index (m_r) of BC coating materials and BC-free particles, mixing state, geometric standard deviation (GSD) and geometric mean diameter (GM) of BC mass size distributions and BC mass concentration. The mixing state takes on two extreme states: core-shell mixed state and external mixed state, while ranges of other parameters change from minimum to maximum values shown in Fig.S5. Results with $\sigma_{sp,sim}$ absolute changes are shown in Fig.S5a, and relative changes are shown in Fig.S5b, with the black circle represents the average case during the short campaign of this study. It shows that m_r is the most important parameter that influence aerosol scattering, while the mixing state also plays a

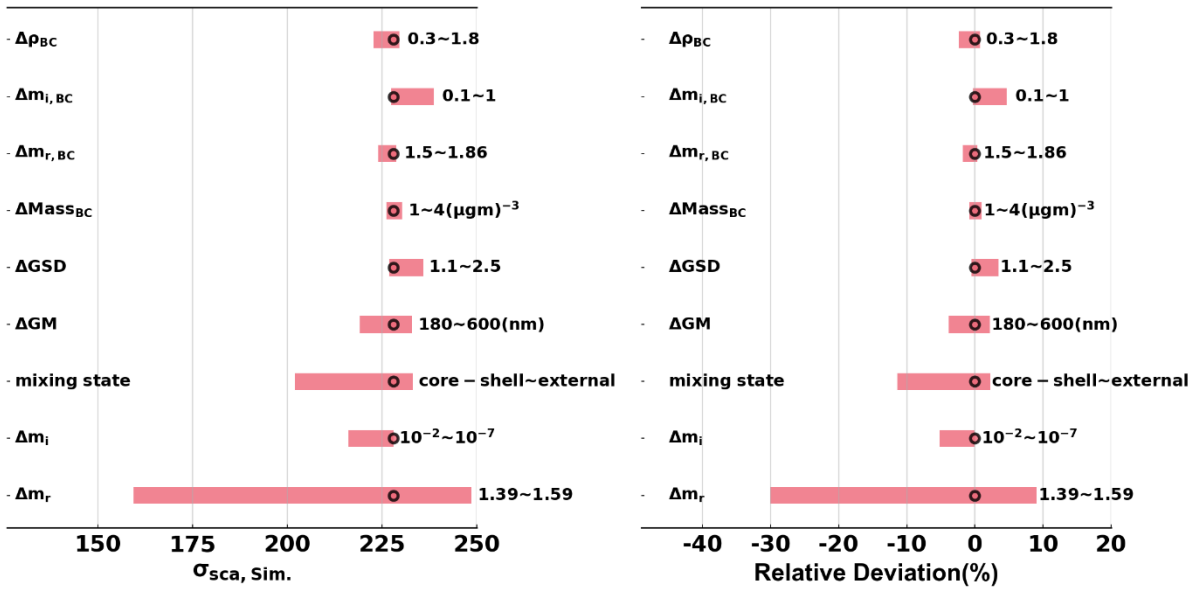

Figure S5. The change and corresponding relative deviation of $\sigma_{sp,sim}$ associated with variations in different input parameters. The range of parameters are show on the right side of bar.

role. However, as demonstrated by results of the first short term campaign, the mixing state would not change in the range of completely core-shell to completely external case, observed mixing state variations can only cause a maxima of ~5% relative changes in aerosol scattering.

Note that, the sensitivity results shown here is somehow contrary to the conclusion draw by Zhao et al. (2019a) that BC mass size distributions, that is GM here, should have comparable impacts with BC mixing states on simulations of aerosol scattering . Here, we explored this further through simulating variations of the ratio ($\sigma_{sp,600}/\sigma_{sp,180}$) between $\sigma_{sp,sim}$ with GM of 600 nm and 180 nm under different R_{ext} (mass ratio of externally mixed BC in total aerosol mass) and R_{csm} (number fraction of internally core-shell mixed BC in total number of internally mixed BC and BC-free particles) conditions, and the results are shown in Fig.S6. It shows that variations of GM have different impacts on aerosol scattering efficiency. For lower R_{csm}, $\sigma_{sp,600}/\sigma_{sp,180}$ is very close to 1, demonstrating that variations in BC mass size distributions have small impacts on aerosol scattering calculations. For R_{csm} equal to 1, which is the case for Zhao et al. (2019a), relative difference between $\sigma_{sp,600}$ and $\sigma_{sp,180}$ could be higher than 10% which share similar magnitudes of influence with BC mixing states. This results explains the inconsistency between findings of Zhao et al. (2019a) with sensitivity results shown in Fig.S5 (the R_{ext} and R_{csm} is also marked on Fig.S6).

A comprehensive sensitivity experiment was further conducted to explore how much variations in these input parameters of optical closure calculations could impact on m_{rc525} retrieval, and results are shown in Fig.S7. It demonstrates that the ratio used for converting measured aerosol

scattering coefficient of TSP ($\sigma_{sp,TSP,525}$) to scattering coefficient of PM_1 ($\sigma_{sp,PM_1,525}$) represents the most important parameter that influence the accuracy of m_{rc525} retrieval.

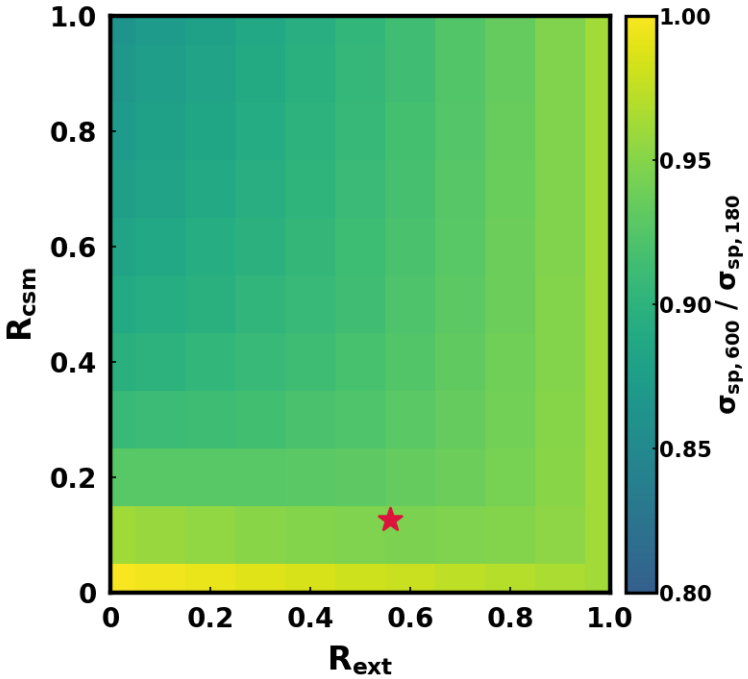

Figure S6. Simulated variations of the ratio $\sigma_{sp,600}/\sigma_{sp,180}$ under different R_{ext} (x-axis) and R_{csm} (y-axis) conditions, colors represent values of $\sigma_{sp,600}/\sigma_{sp,180}$.

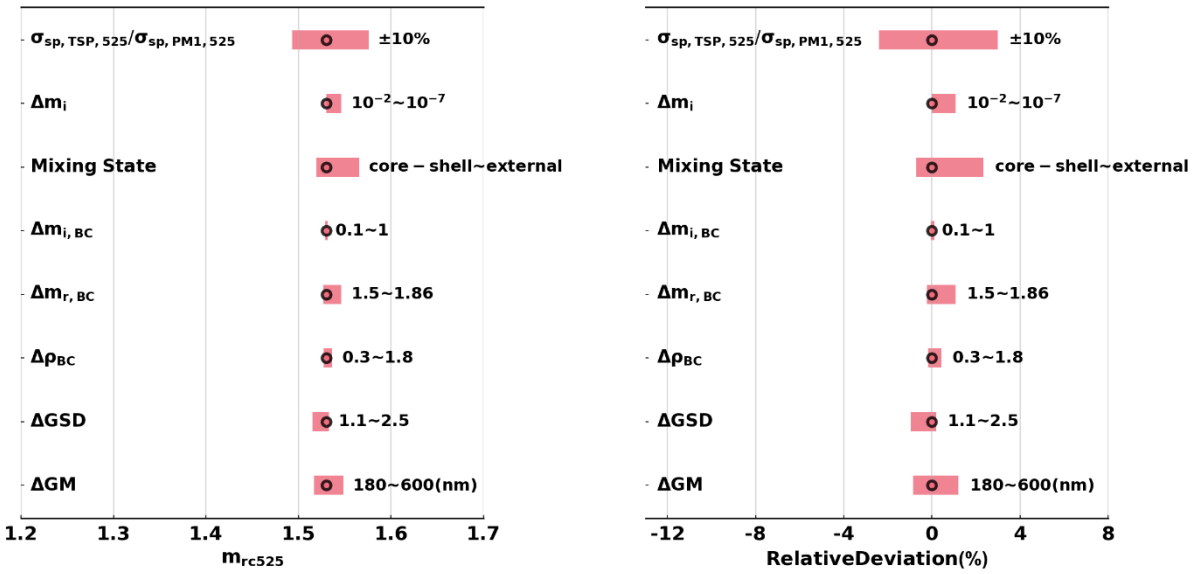

Figure S7. The change and corresponding relative deviation of retrieved m_{rc525} associated with variations in different input parameters. The range of parameters are show on the right side of bar. The sensitivity study was performed using average PNSD, BC mass size distributions and mixing states in the first short campaign.

6. Test experiment on using the volume mixing rule to retrieve m_{rc525} of POA and SOA if POA and SOA is externally mixed

To evaluate the applicability of the volume mixing rule under conditions where POA and SOA are externally mixed, simulations were conducted following these steps, and the : (1) Assume the geometric mean of the volume size distribution of POA is 250 nm and the geometric standard deviation is 1.5; (2) Assume the geometric mean of the volume size distribution of SOA is 450 nm and the geometric standard deviation is 1.5; (3) Define the m_r of POA at 525 nm ($m_{r525,POA}$) to range from 1.34 to 1.54; (4) Define the m_r of SOA at 525 nm ($m_{r525,SOA}$) to range from 1.43 to 1.63; (5) For each $m_{r525,POA}$ and $m_{r525,SOA}$ pair, assume SOA mass concentration of 10 μg/m3 and ranging POA mass concentrations from 5 to 15 μg/m3; (6) For each $m_{r525,POA}$ and $m_{r525,SOA}$ pair, calculate the summed aerosol scattering coefficients at 525 nm based on the combined contributions of POA and SOA, then derive corresponding m_{rc525} values; (7) Retrieve the m_{rc525} of POA and SOA using the volume mixing rule.

The introduced procedures mean that for each $m_{r525,POA}$ and $m_{r525,POA}$ pair, aerosol scattering under different POA and SOA fractions were simulated and different m_{rc525} values that could be retrieved using simulated total aerosol scattering and particle number size distributions. For each POA and SOA condition, the volume of POA ans SOA are converted from assumed mass concentrations using densities of POA (1.0 g/cm³) and SOA (1.3 g/cm³ for convenience).

The volume size distributions of POA and SOA follow lognormal distributions:

$$\mathrm{d}V_x/\mathrm{dlogDp} = \frac{V_x}{\sqrt{2\pi}\log(\sigma_{\mathrm{g,x}})}\exp\left[-\frac{(\log(\mathrm{D}_p)-\log(\mathrm{D}_{\mathrm{g,x}}))^2}{2\log^2\sigma_{\mathrm{g,x}}}\right] \quad (7)$$

where x corresponding to SOA and POA, V_x represents corresponding total volume concentration derived from mass concentrations, $\sigma_{\mathrm{g,x}}$ represents corresponding geometrical mean, $\sigma_{\mathrm{g,x}}$ represents corresponding geometric standard deviation.

$$\mathrm{N(logDp)_{POA}} = \mathrm{d}V_{POA}/\mathrm{dlogDp}/V(\mathrm{Dp}) \quad (8)$$

$$\mathrm{N(logDp)_{SOA}} = \mathrm{d}V_{POA}/\mathrm{dlogDp}/V(\mathrm{Dp}) \quad (9)$$

Where $V(\mathrm{Dp})$ is the volume one single particle with diameter of Dp.

$$\sigma_{sp,POA}(525) = \int Q_{sp}(Dp, \tilde{m}_{POA}, 525) * (\frac{\pi Dp^2}{4}) * \mathrm{N(logDp)_{POA}} * dlogDp \quad (10)$$

Where $\tilde{m}_{POA} = m_{r525,POA} + i \times 10^{-7}$, and $Q_{sp,POA}$ is the scattering efficiency, 10^{-7} for the imaginary part for consistency with the optical closure calculations in Sect 2.3.

$$\sigma_{sp,SOA}(525) = \int Q_{sp}(Dp, \tilde{m}_{SOA}, 525) * (\frac{\pi Dp^2}{4}) * \mathrm{N(logDp)_{SOA}} * dlogDp \quad (11)$$

Where $\tilde{m}_{SOA}$= $m_{r525,SOA} + i \times 10^{-7}$, and Q_{sp} is the scattering efficiency.

Then:

$$\sigma_{sp}(525) = \sigma_{sp,POA}(525) + \sigma_{sp,SOA}(525) \quad (12)$$

And, size distributions of SOA and POA populations:

$$\mathrm{N(logDp)} = \mathrm{N(logDp)}_{POA} + \mathrm{N(logDp)_{SOA}} \quad (13)$$

Finally, the m_{rc525} of the total aerosol populations could be retrieved iteratively using the following form equation:

$$\sigma_{sp}(525) = \int Q_{sp}(Dp, \tilde{m}_{c}, 525) * (\frac{\pi Dp^2}{4}) * \mathrm{N(logDp)} * dlogDp \quad (14)$$

Where $\tilde{m}_{c}$= $m_{rc525} + i \times 10^{-7}$,

For each $m_{r525,POA}$ and $m_{r525,POA}$ pair, a list of data pairs of retrieved m_{rc525} as well as volume fractions of SOA and POA could be obtained. Then $m_{rc525,POA}$ and $m_{rc525,POA}$ could be retrieved using the volume mixing rule with retrieved m_{rc525} points and corresponding volume fractions of POA and SOA ($f_{V,POA}$ and $f_{V,SOA}$) as inputs of the following multilinear regression formula:

$$m_{rc525} = m_{rc525,POA} \times f_{V,POA} + m_{rc525,SOA} \times f_{V,SOA} \quad (15)$$

For all $m_{r525,POA}$ and $m_{r525,POA}$ pairs, the comparison results between the retrieved $m_{rc525,POA}$ and $m_{rc525,SOA}$ values and their assumed counterparts are shown in Fig. S9. Results demonstrate that in general, the retrieved m_{rc525} values closely match the original values, with deviations averaging less than 2%. These findings confirm the applicability of the volume mixing rule under conditions where POA and SOA are externally mixed.

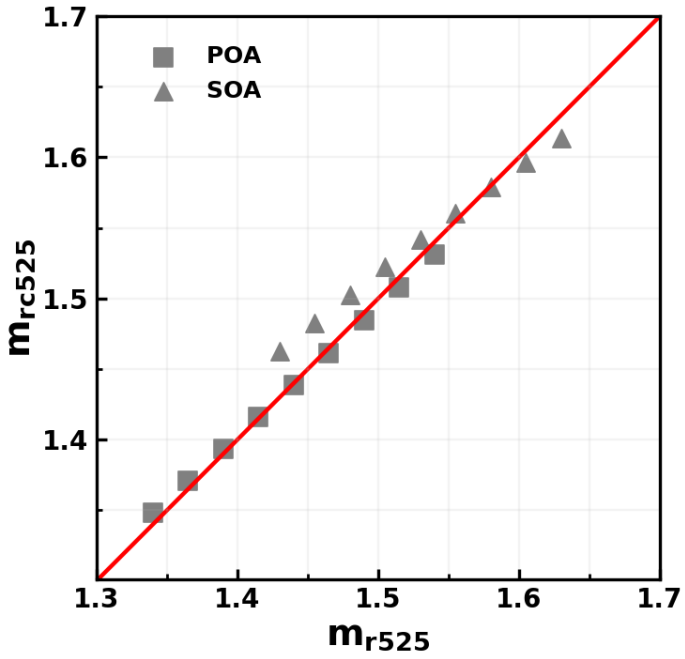

Figure S8. Comparison between original m_{r525} and m_{rc525} retrieved using the volume mixing rule for both POA and SOA in simulations where SOA and POA are externally mixed.

7. Other supplementary Figures

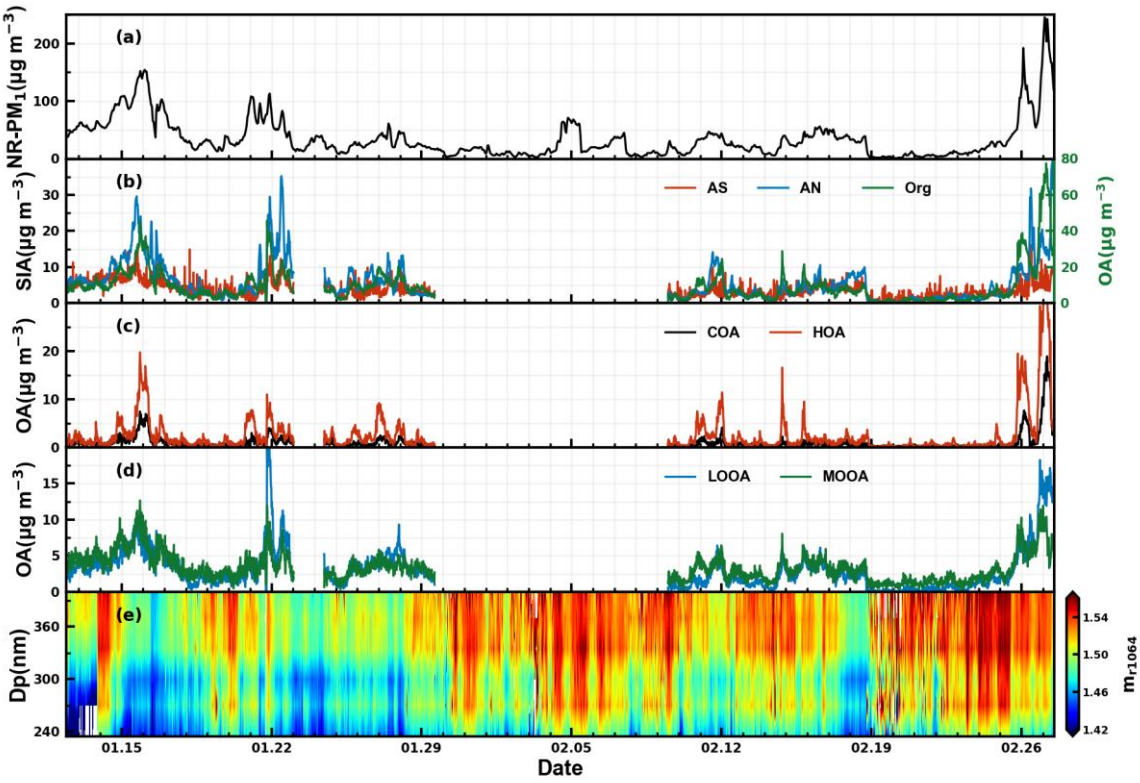

Figure S9. Time series of aerosol components and size dependent real part of refractive index (m_{r1064}) retrieved using DMA-SP2 measurements at different particle size from January 12 to February 27, 2022.

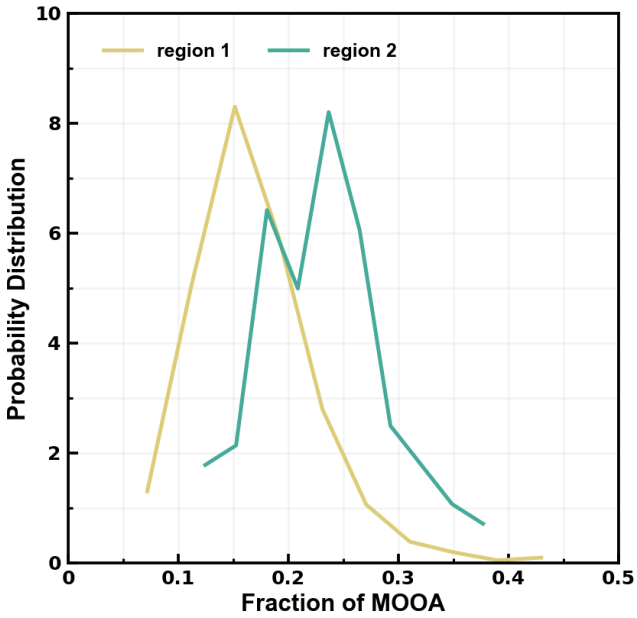

Figure S10. Probability distributions of MOOA mass fractions in total NR-PM1 in two rectangular regions of Fig.1b

263

264

265

266

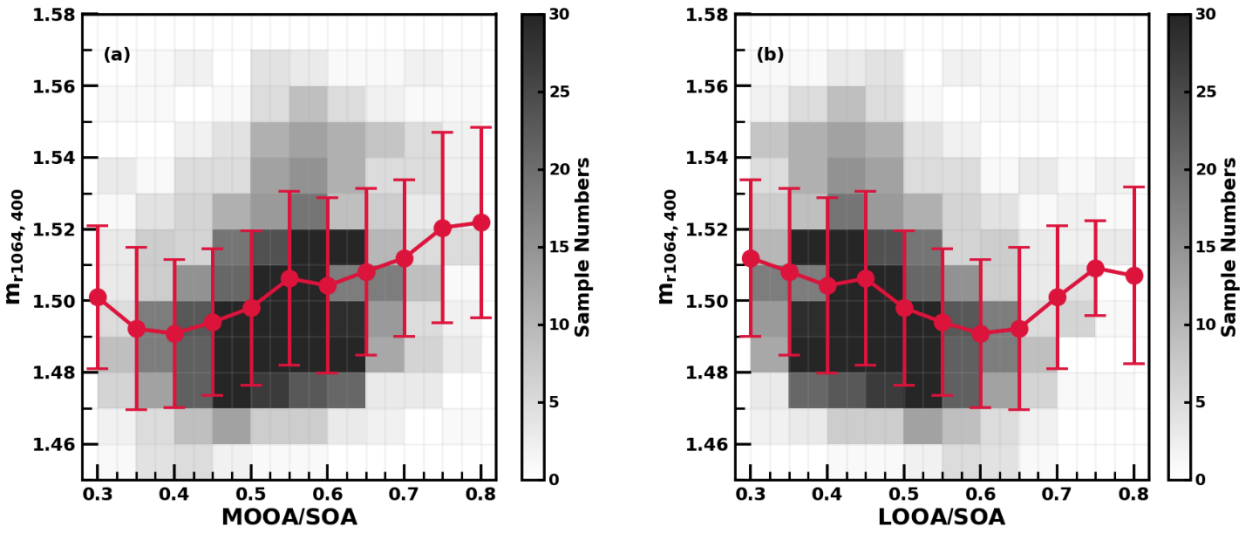

Figure S11. $m_{r1064,400}$ variations with the ratio **(a)**MOOA to SOA (b)LOOA SOA derived from factor1 and factor 2, which account for over 70% of all factors at 400 nm. The intensity of colors indicates the number of samples, while red spots and error bars represent average values and standard deviations.

267

268

Reference

Cheng, Y., Wiedensohler, A., Eichler, H., Heintzenberg, J., Tesche, M., Ansmann, A., Wendisch, M., Su, H., Althausen, D., and Herrmann, H.: Relative humidity dependence of aerosol optical properties and direct radiative forcing in the surface boundary layer at Xinken in Pearl River Delta of China: An observation based numerical study, Atmospheric Environment, 42, 6373-6397, 2008.

Kuang, Y., He, Y., Xu, W., Yuan, B., Zhang, G., Ma, Z., Wu, C., Wang, C., Wang, S., Zhang, S., Tao, J., Ma, N., Su, H., Cheng, Y., Shao, M., and Sun, Y.: Photochemical Aqueous-Phase Reactions Induce Rapid Daytime Formation of Oxygenated Organic Aerosol on the North China Plain, Environmental science & technology, 54, 3849-3860, 10.1021/acs.est.9b06836, 2020.

Kuang, Y., Xu, W., Tao, J., Luo, B., Liu, L., Xu, H., Xu, W., Xue, B., Zhai, M., Liu, P., and Sun, Y.: Divergent Impacts of Biomass Burning and Fossil Fuel Combustion Aerosols on Fog-Cloud Microphysics and Chemistry: Novel Insights From Advanced Aerosol-Fog Sampling, Geophysical Research Letters, 51, e2023GL107147, https://doi.org/10.1029/2023GL107147, 2024.

Müller, T., Laborde, M., Kassell, G., and Wiedensohler, A.: Design and performance of a three-wavelength LED-based total scatter and backscatter integrating nephelometer, Atmos. Meas. Tech., 4, 1291-1303, 10.5194/amt-4-1291-2011, 2011.

Ma, N., Zhao, C. S., Nowak, A., Müller, T., Pfeifer, S., Cheng, Y. F., Deng, Z. Z., Liu, P. F., Xu, W. Y., Ran, L., Yan, P., Göbel, T., Hallbauer, E., Mildenberger, K., Henning, S., Yu, J., Chen, L. L., Zhou, X. J., Stratmann, F., and Wiedensohler, A.: Aerosol optical properties in the North China Plain during HaChi campaign: an in-situ optical closure study, Atmos. Chem. Phys., 11, 5959-5973, 10.5194/acp-11-5959-2011, 2011.

Tan, H., Yin, Y., Gu, X., Li, F., Chan, P. W., Xu, H., Deng, X., and Wan, Q.: An observational study of the hygroscopic properties of aerosols over the Pearl River Delta region, Atmospheric Environment, 77, 817-826, https://doi.org/10.1016/j.atmosenv.2013.05.049, 2013.

Wex, H., Neusüß, C., Wendisch, M., Stratmann, F., Koziar, C., Keil, A., Wiedensohler, A., and Ebert, M.: Particle scattering, backscattering, and absorption coefficients: An in situ closure and sensitivity study, Journal of Geophysical Research: Atmospheres, 107, LAC 4-1-LAC 4-18, https://doi.org/10.1029/2000JD000234, 2002.

Xu, W., Kuang, Y., Xu, W., Zhang, Z., Luo, B., Zhang, X., Tao, J., Qiao, H., Liu, L., and Sun, Y.: Hygroscopic growth and activation changed submicron aerosol composition and properties in the North China Plain, Atmos. Chem. Phys., 24, 9387-9399, 10.5194/acp-24-9387-2024, 2024.

Zhao, G., Tao, J., Kuang, Y., Shen, C., Yu, Y., and Zhao, C.: Role of black carbon mass size distribution in the direct aerosol radiative forcing, Atmos. Chem. Phys., 19, 13175-13188, 10.5194/acp-19-13175-2019, 2019a.

Zhao, G., Zhao, W., and Zhao, C.: Method to measure the size-resolved real part of aerosol refractive index using differential mobility analyzer in tandem with single-particle soot photometer, Atmos. Meas. Tech., 12, 3541-3550, 10.5194/amt-12-3541-2019, 2019b.

Zhou, Y., Ma, N., Wang, Q., Wang, Z., Chen, C., Tao, J., Hong, J., Peng, L., He, Y., Xie, L., Zhu, S., Zhang, Y., Li, G., Xu, W., Cheng, P., Kuhn, U., Zhou, G., Fu, P., Zhang, Q., Su, H., and Cheng, Y.: Bimodal distribution of size-resolved particle effective density: results from a short campaign in a rural environment over the North China Plain, Atmos. Chem. Phys., 22, 2029-2047, 10.5194/acp-22-2029-2022, 2022.